Computational prediction and experimental realisation of earth abundant transparent conducting oxide Ga-doped ZnSb$_2$O$_6$

Adam J. Jackson[1], Benjamin J. Parrett[2,3], Joe Willis[3,4,5], Alex M. Ganose[6], W. W. Winnie Leung[4], Yuhan Liu[4], Benjamin A. D. Williamson[7], Timur K. Kim[2,3], Moritz Hoesch[2,3], Larissa Ishibe-Veiga[2,3], Raman Kalra[4], Jens Neu[8], Charles A. Schmuttenmaer[8], Tien-Lin Lee[3], Anna Regoutz[3,4], Tim D. Veal[9], Robert G. Palgrave[4], Robin Perry[10,11], and David O. Scanlon[4,5]

[1]Scientific Computing Department, Science and Technology Facilities Council, Rutherford Appleton Laboratory, Harwell Science and Innovation Campus, Didcot, OX11 0QX, UK.
[2]London Centre for Nanotechnology and Dept of Physics and Astronomy, University College London, London, WC1E 6BT, UK.
[3]Diamond Light Source Ltd., Harwell Science and Innovation Campus, Didcot, Oxfordshire, OX11 0DE, UK.
[4]Dept of Chemistry, University College London, 20 Gordon St, London, WC1H 0AJ, UK.
[5]Thomas Young Centre, University College London, Gower St, London, WC1E 6BT, UK.
[6]Dept of Materials, Imperial College London, Exhibition Rd, London, SW7 2AZ, UK.
[7]Dept of Materials Science and Engineering, Norweigan University of Science and Technology (NTNU), Trondheim, 7491, Norway
[8]Dept of Chemistry, Yale University, New Haven, Connecticut, 06520-8107, USA.
[9]Dept of Physics and Stephenson Institute for Renewable Energy, University of Liverpool, Liverpool, L69 7ZF, UK.
[10]London Centre for Nanotechnology and UCL Institute for Materials Discovery, University College London, London, WC1e 6BT, UK.
[11]ISIS Pulsed Neutron and Muon Source, Rutherford Appleton Laboratory, Harwell Science and Innovation Campus, Didcot, Oxfordshire, OX11 0QX, UK.

March 16, 2022

Correspondence

Correspondence should be addressed to `d.scanlon@ucl.ac.uk`

Abstract

Transparent conducting oxides have become ubiquitous in modern opto-electronics. However, the number of oxides that are transparent to visible light and have the metallic-like conductivity necessary for transparent conducting oxide applications is limited to a handful of systems that have been known for the past forty years. In this work, we use hybrid density functional theory and defect chemistry analysis to demonstrate that tri-rutile zinc antimonate, ZnSb$_2$O$_6$, is an ideal transparent conducting oxide, and identify gallium as the optimal dopant to yield high conductivity and transparency. To validate our computational predictions, we have synthesised both powder samples and single crystals of Ga-doped ZnSb$_2$O$_6$ which conclusively show behaviour consistent with a degenerate transparent conducting oxide. This study demonstrates the possibility of a family of Sb(V) containing oxides for transparent conducting oxide and power electronics applications.

1 Introduction

Transparent conducting oxides (TCOs) are an essential component of modern photovoltaic and display screen technologies. Sn-doped In$_2$O$_3$ (ITO) displays the superior opto-electronic properties among the

industrially used TCOs; it has been reported to possess resistivities as low as $8 \times 10^{-5}\,\Omega\,cm$, mobilities that exceed $50\,cm^2\,V^{-1}\,s^{-1}$, carrier concentrations on the order of $1 \times 10^{21}\,cm^{-3}$, all whilst retaining over 90% transparency to visible light.[1] The more earth abundant TCOs, such as F-doped SnO_2 (FTO)[2] or Al-doped ZnO (AZO)[3] display mobilities and conductivities below that of ITO, which limits their application in display screen technologies. However, ITO is not considered for large area applications such as in photovoltaics or smart window applications, despite recent improvements in the efficiency of indium based TCOs via innovative doping (Mo and Ce),[4,5,6] due to the expense and scarcity of indium. Therefore, there is a drive to try to increase the performance of the known earth abundant TCOs,[7,8] or more unusually, to discover new TCOs. The last "new" TCOs to be reported were La-doped $BaSnO_3$ in 2012,[9] an oxide that had been studied as a TCO for decades without success until the synthesis of a high quality, high-mobility single crystal, and the correlated metals $SrVO_3$ and $CaVO_3$ in 2015.[10]

In terms of materials design, the common trend in the majority of the effective n-type TCOs is the presence of post-transition metal cations with the electronic structure $(n-1)d^{10}ns^0np^0$. In these materials, the s orbitals of the cation hybridise with oxygen s states yielding conduction bands with low electron effective masses.[11] Indeed the majority of the cations in the industrially relevant TCOs are limited to groups 12, 13 and 14 of the periodic table. In an early investigation of ternary oxides, Shannon et al noted that edge-sharing Cd^{2+}, In^{3+} and Sn^{4+} octahedra were a feature of common transparent conductors.[12]

In 2004, Mizoguchi and Woodward employed a joint theory and experimental study to investigate the necessity for edge-sharing octahedral connectivity when designing n-type TCOs.[13] They found that edge-sharing is not a prerequisite, and corner sharing can also provide excellent dispersion of the conduction band, such as in $BaSnO_3$.[9] Interestingly, they identified some ternary oxides containing Sb(V) and Bi(V) which displayed reasonable curvature of the conduction band minimum,[13] including tri-rutile zinc antimonate ($ZnSb_2O_6$). It should be noted that group 15 cations in their highest oxidation states possess the same $(n-1)d^{10}ns^0np^0$ electronic structure as the cations in the common, successful TCOs.

Despite the identification of $ZnSb_2O_6$ as a potential TCO, the material has not received a huge amount of attention. It had previously been studied by Kikuchi et al as a potential TCO and thermoelectric in 2005,[14] but it was only ever produced as a powder and little data on the optoelectronic properties were published. Hautier et al identified $ZnSb_2O_6$ as a potential low electron effective mass TCO in their computational screening study of 2014, calling on the solid-state community for further computational and experimental investigation. Meanwhile, Li et al briefly investigated it as a potential anode for Li battery technology.[15] However, no high quality single crystals of $ZnSb_2O_6$ have been reported, and its full potential as a transparent conductor is yet to be assessed.

In this work, we investigated the crystal and electronic structure of $ZnSb_2O_6$ with hybrid density functional theory, and validated this description with quasi-particle self-consistent GW theory (Green's function, G with a screened Coulomb interaction, W). A full intrinsic defect analysis was performed that showed when nominally undoped, $ZnSb_2O_6$ does not fulfil the Mott criterion for metallic-like conductivity. We then considered three extrinsic dopants, and demonstrated that Ga is the optimum electron donor in $ZnSb_2O_6$. Using this knowledge, we successfully grew powder and single crystal samples of Ga-doped $ZnSb_2O_6$, which displayed excellent optical transparency (>99%), electron mobility between $40\,cm^2\,V^{-1}\,s^{-1}$ to $50\,cm^2\,V^{-1}\,s^{-1}$ and carrier concentrations on the order of $2 \times 10^{20}\,cm^{-3}$. The results presented in this study demonstrate that Ga-doped $ZnSb_2O_6$ displays all the indicators of a high-performance transparent conductor, and serve as an important proof-of-concept for Sb(V) based TCO design.

2 Results

2.1 Crystal Structure

$ZnSb_2O_6$ crystallises in a tri-rutile structure, belonging to the $P4_2/mnm$ space group, as shown in Figure 1. The structure consists of ZnO_6 and SbO_6 edge-sharing octahedra in the order ZnO_6-SbO_6-SbO_6 along the c-axis, with corner-sharing octahedra present throughout the a-b planes. It has

Method	a / Å	c / Å	a/c
PXRD*	4.6793	9.2906	0.5037
PBE0*	4.6740	9.2585	0.5048
PBEsol*	4.6921	9.3388	0.5024
Bystroem et al[18]	4.67	9.26	0.50
Nishiyama et al[19]	4.668	9.265	0.504
Kikuchi et al[14]	4.68	9.29	0.50

Table 1: Lattice parameters of $ZnSb_2O_6$ resolved from experiment and simulations. Asterisks denote results from this work.

tetragonal unit cell parameters, a summary of which is provided in Table 1 for a range of exchange correlation functionals and experiments. The XRD results show an excellent fit to the $P4_2/mnm$ space group, as can be seen in the XRD pattern in Figure 2, and the PBE0 lattice parameters are in good agreement with room temperature XRD results. The PBEsol lattice parameters are slightly overestimated, which is typical of the generalised gradient approximation (GGA) implementation in DFT.[16]
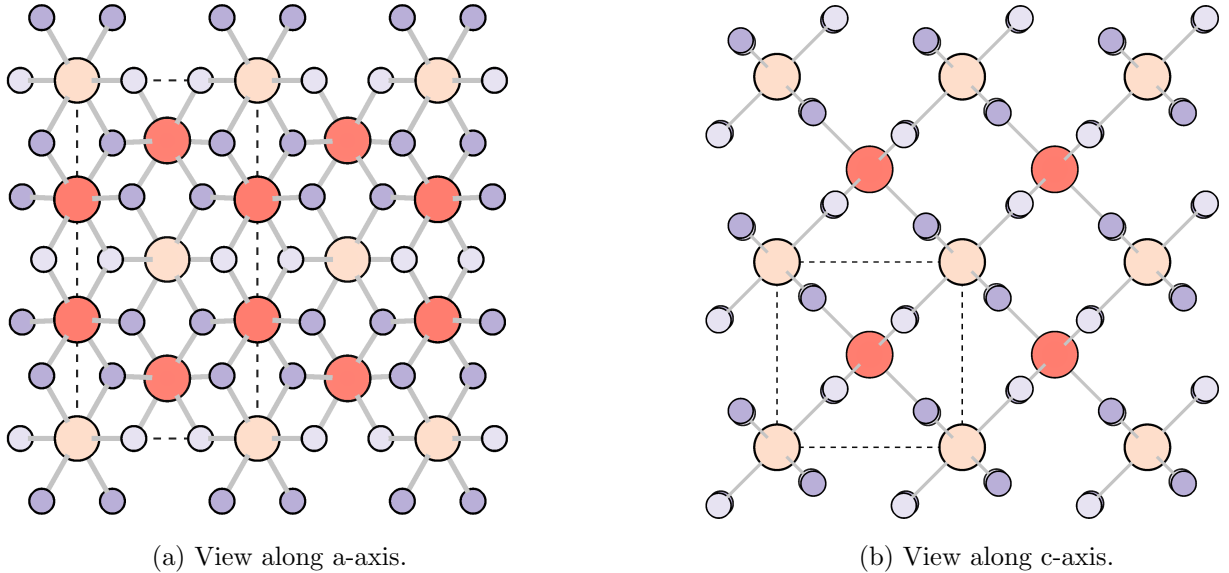

(a) View along a-axis.

(b) View along c-axis.

Figure 1: Crystal structure of $ZnSb_2O_6$, space group $P4_2/mnm$. Zn, Sb and O atoms are shown in pale orange, dark orange and blue, respectively. There are two distinct anion sites, denoted by different shades of blue. Visualised using VESTA.[17]

Doping with Ga causes a systematic shift in the Bragg peaks to higher angles compared to undoped samples, illustrated in Figure 14, indicating a shrinkage in cell size. This observation is consistent with substituting Ga with Zn in an octahedral environment, as Ga has a smaller ionic radius (0.62 Å) compared to Zn (0.74 Å).[20] The unit cell volumes also shift from 201.78 Å^3 to 201.48 Å^3 after Ga doping, extracted by Rietveld refinement using the GSAS-II software.[21] These observations are consistent with a solid solution of gallium replacing zinc in the tri-rutile structure, with no detectable phase separation.
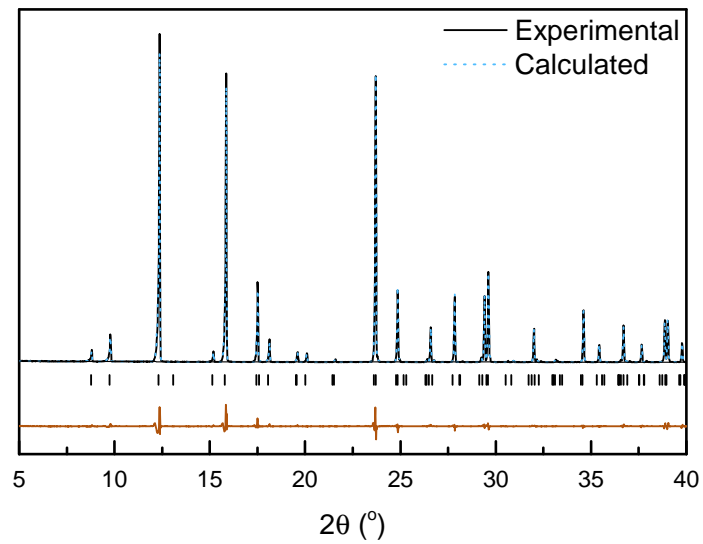
Figure 2: Powder x-ray diffraction pattern for annealed $ZnSb_2O_6$. Dashed line indicates Rietveld refinement for $P4_2/mnm$ tri-rutile structure; difference between fit and data is shown below peak positions.

2.2 Electronic Structure

The electronic band structure of $ZnSb_2O_6$ was calculated using the PBE0 functional and is displayed in Figure 3a. A direct band gap of $3.54\,eV$ at Γ is observed, with relatively high dispersion at the conduction band minimum (CBM), ideal for a prospective transparent conductor. The electron effective mass in the $\Gamma \to X$ and $\Gamma \to M$ directions is $0.27m_e$, and improves further along $\Gamma \to Z$ (in the c-direction) to $0.22m_e$, in reasonable agreement with the electron effective masses screened by Hautier et al.[22] The high dispersion originates from the good overlap of Sb $5s$ orbitals, which are the main contributor to the CBM density of states, with Zn and O s states. Qualitatively, the conduction band shape is in good agreement with previous GGA-DFT calculations, while the hybrid functional corrects for the systematic underestimation of the band gap,[22] and is competitive with state-of-the-art TCOs In_2O_3, SnO_2, ZnO and $BaSnO_3$.[2,8,7,23] Figure 3b shows the band structure computed with hQSGW theory, which shows a small (3%) decrease in the direct band gap to $3.41\,eV$, with the electron effective masses unchanged. Ultimately, the PBE0 description is sufficient, accurately describing the nature of the band gap compared to the next level of theory, and is used subsequently for defect calculations.
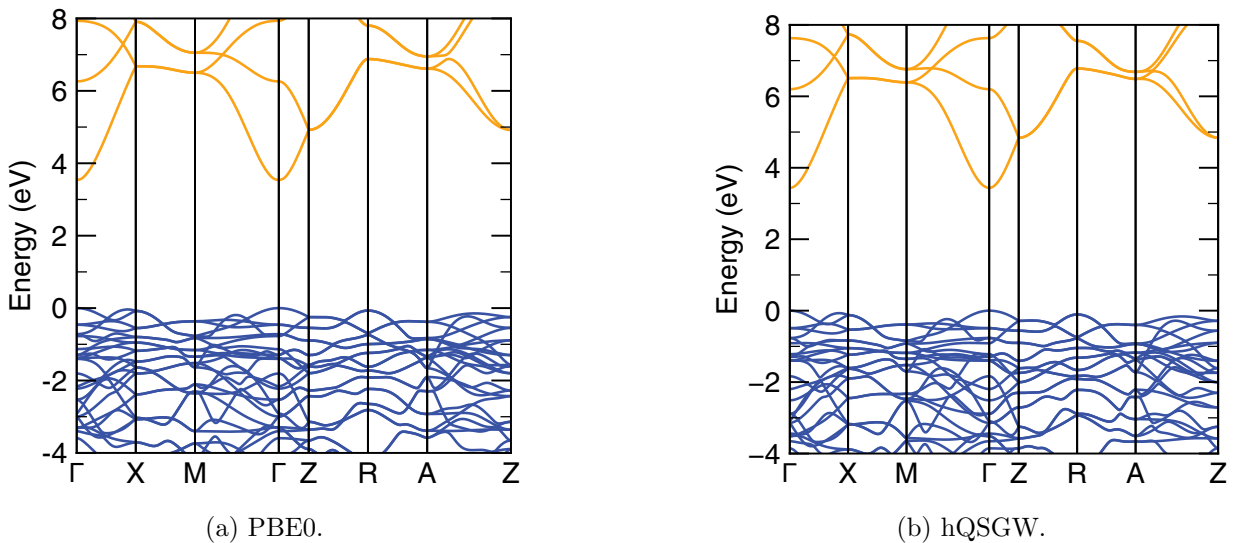

(a) PBE0. (b) hQSGW.

Figure 3: Electronic band structures of $ZnSb_2O_6$ computed with (a) hybrid DFT (PBE0); (b) quasiparticle self-consistent GW using 80% scaling of self-energy (hQSGW).

Simulated and experimental photoelectron spectra of the valence band of $ZnSb_2O_6$ are shown in Figure 4, plotted using GALORE.[24,25] The simulated spectrum is obtained from the PBE0 density of states calculation, where the orbital contributions were weighted with tabulated photoionisation cross-sections and broadened with Guassian and Lorentzian functions to match the experimental lineshapes. The spectra were approximately aligned by the first peak position. The key valence band features in Figure 4 are in agreement: an initial onset mainly comprised of Zn $3d$, Sb $4d$ O $2p$ states followed by a small dip and a large sharp peak assigned to Zn $3d$ states. However, the position of this peak is under-bound by approximately $2\,eV$. Similar discrepancies have been observed with hybrid DFT for Zn $3d$ states in ZnO and for Sn $4d$ states in SnO_2.[26,27]
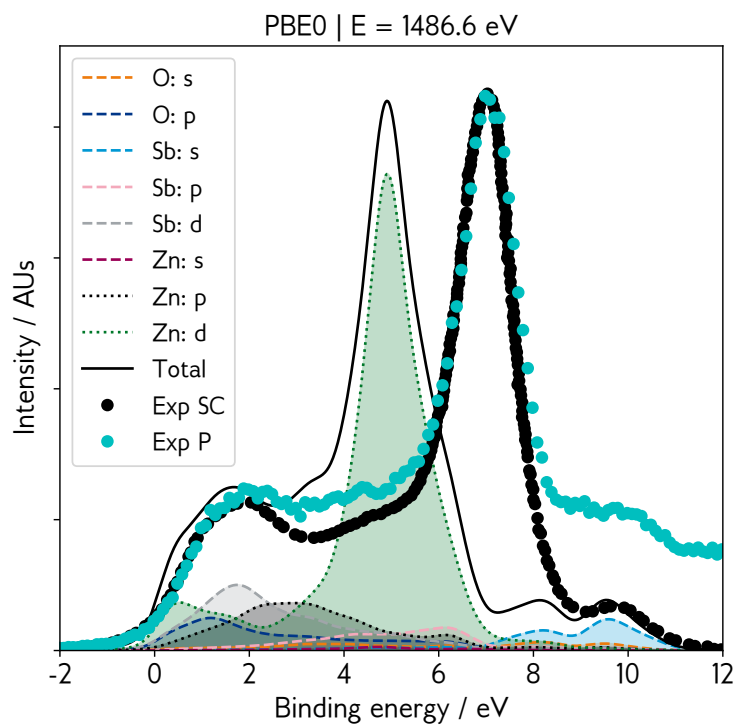
Figure 4: Simulated valence band spectra using the PBE0 functional, with a Gaussian broadening of 0.6 eV, Lorentzian broadening of 0.2 eV and weighting by photoionisation cross-sections for E = 1486.6 eV. Experimental data is overlaid in black for a single crystal and cyan for a powder sample.

2.3 Defect Chemistry

While the electronic structure of $ZnSb_2O_6$ is a promising indicator of high transparent conducting performance, it is the defect chemistry that will ultimately control the electrical properties of the system. Degenerate conductivity is achieved when the charge carrier concentration exceeds the Mott criterion:[28,29,30,31]

$$n_{\text{Mott}} > \left(\frac{0.26}{a_0}\right)^3 \quad \text{where} \quad a_0 = \frac{4\pi\epsilon_0\epsilon_\infty\hbar^2}{m^*e^2} \quad \text{and} \quad \frac{1}{m^*} = \frac{1}{m_e^*} + \frac{1}{m_h^*} \tag{1}$$

which for $ZnSb_2O_6$ is $2.6 \times 10^{18}\,\text{cm}^{-3}$, where a_0 is the effective Bohr radius ($1.89 \times 10^{-9}\,\text{m}$), ϵ_0 is the static dielectric constant (7.74), and m^* is the reduced effective mass ($1.97 \times 10^{-31}\,\text{kg}$).
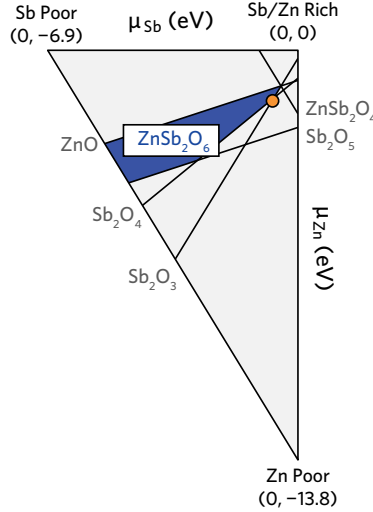

Figure 5: Thermodynamic stability region of $ZnSb_2O_6$, calculated using CPLAP.[32] The orange marker denotes the most n-type growth conditions, the chemical potential limits at which the defect formation energies in this work are reported.

We first identify the thermodynamic stability region (blue) of $ZnSb_2O_6$ with respect to its competing phases in Figure 5. Using the chemical potential limits bounded by this region, the transition level diagram for intrinsic defects, namely zinc, antimony and two non-equivalent oxygen vacancies (V_{Zn}, V_{Sb} and V_O), cation substitutions (Zn_{Sb} and Sb_{Zn}) and various interstitial sites (Zn_i, Sb_i and O_i), is calculated and displayed in Figure 6a.

The intrinsic defect chemistry does not support degenerate n-type behaviour. V_O acts as a deep donor defect, in line with the behaviour observed in established TCOs such as In_2O_3, SnO_2 and ZnO (CdO being the notable exception),[33,5,34,8,35] and is discussed in greater detail in the SI. The Sb_{Zn} substitution is the next lowest energy species, but it is charge compensated by V_{Zn} just below the CBM, pinning the Fermi level in the gap. We can predict the position of the Fermi level and charge carrier concentrations through a self-consistent Fermi level (SCFL) analysis – the synthesis temperature of $ZnSb_2O_6$ is $\sim 1400\,\text{K}$, so by fixing the defect concentrations present at this temperature and re-calculating the SCFL at room temperature, we can predict room temperature experimental charge carrier concentrations. Undoped $ZnSb_2O_6$ is predicted to have $3.1 \times 10^{16}\,\text{cm}^{-3}$ charger carriers (significantly below the Mott criterion), with the SCFL to be $0.13\,\text{eV}$ below the conduction band edge, precluding undoped $ZnSb_2O_6$ from metallic-like conductivity. From experiment, we measure $5.0 \times 10^{17}\,\text{cm}^{-3}$ carriers in undoped crystals, around an order of magnitude more than predicted, and low conductivity (around $2\,\text{S/cm}$) in both powder and single crystal samples. The larger carrier concentration measured in the crystals is likely due to adventitious H-doping during synthesis, as well as trace amounts of other impurities that could contribute electrons (such as Cl from the carrier gas), and is in qualitative agreement with the SCFL analysis – that when nominally undoped, $ZnSb_2O_6$ does not display metallic conductivity.
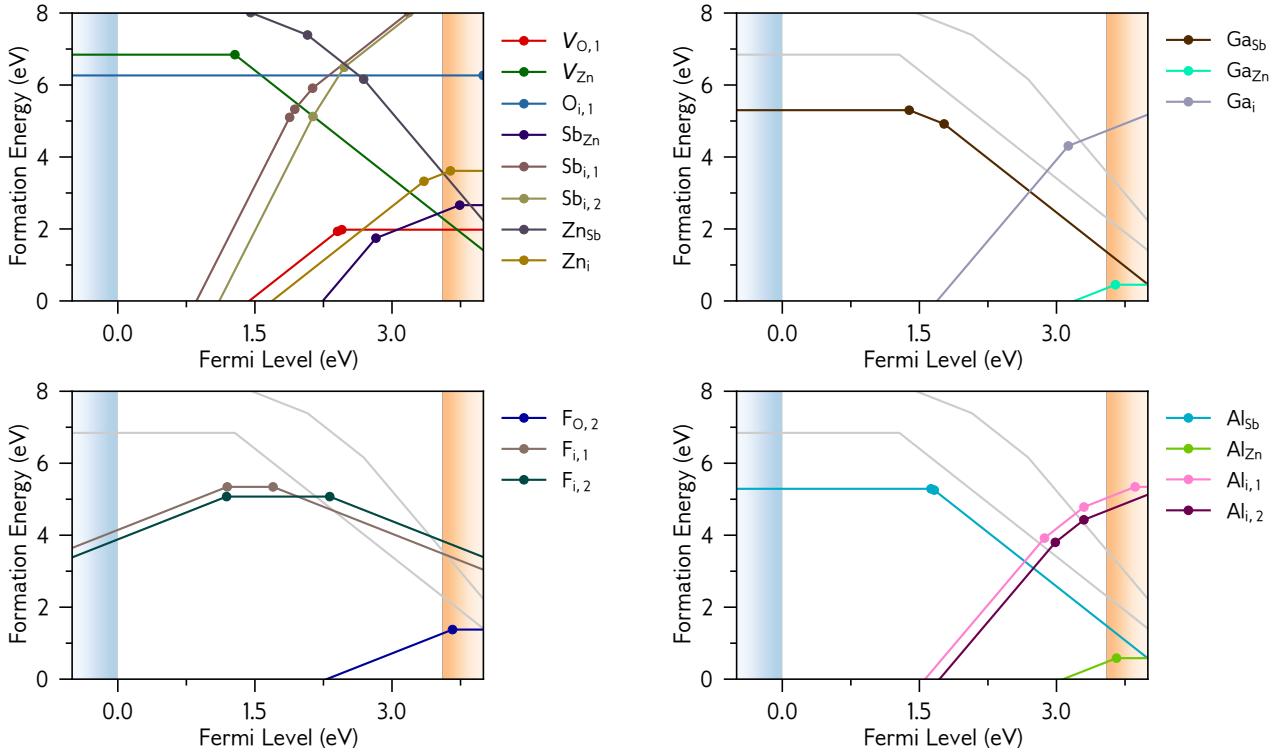
Figure 6: Moving from left to right across the top and then bottom rows, transition level diagrams for (a) intrinsic defects only; (b) doping with gallium; (c) doping with fluorine; (d) doping with aluminium. The blue and orange shaded regions denote the valence and conduction bands, respectively. Each coloured line represents a different defect, and the gradient of that line denotes the charge state. Filled circles represent transition levels, where two charge states are in thermodynamic equilibrium. Calculated using AIDE. For V_O, O_i, Zn_i and Ga_i, only the lower energy of the two non-equivalent defect sites are plotted.

Next, we investigated Ga, Al and F as potential electron donors in $ZnSb_2O_6$ in order to drive the Fermi level up into the conduction band and realise degenerate conductivity. The transition level diagram for each dopant is shown in Figure 6b-d, where we find that Ga_{Zn} and Al_{Zn} are low energy donors, with formation energies of 0.45 eV and 0.58 eV in their neutral charge states, respectively. In both cases, the dopant interstitial defects are rather high in energy (around 5 eV at the CBM), and are charge compensated by their respective dopant-substitutions onto the Sb site. F_O anion substitutions have higher formation energies of 1.38 eV and 1.46 eV for the inequivalent oxygen sites, while the F interstitials do not donate electrons to the conduction band. Crucially, we find that the native p-type defects, V_{Zn} and Zn_{Sb} are too high in energy to charge compensate Ga_{Zn}, Al_{Zn} and F_O. We complete the same SCFL analysis as before for each case, and find that Ga emerges as the superior dopant with a predicted room temperature charge carrier concentration of $3.4 \times 10^{19}\,\mathrm{cm}^{-3}$ and a SCFL of 3.69 eV (0.15 eV above the CBM), thereby predicting degenerate conductivity. For Al and F, the predicted charge carrier concentrations are $3.2 \times 10^{17}\,\mathrm{cm}^{-3}$ and $7.2 \times 10^{18}\,\mathrm{cm}^{-3}$, with the SCFL sitting above the CBM in both cases. Experimentally, we record carrier concentrations of $8.9 \times 10^{19}\,\mathrm{cm}^{-3}$, $2.0 \times 10^{20}\,\mathrm{cm}^{-3}$ and $2.4 \times 10^{20}\,\mathrm{cm}^{-3}$ for 1%, 3% and 8% Ga-doping in single crystals. The presence of adventitious H is the most likely origin of discrepancy, but again we find qualitative agreement with the SCFL analysis. Conductivity rises by several orders of magnitude in the single crystals to $526\,\mathrm{S\,cm}^{-1}$, $1230\,\mathrm{S\,cm}^{-1}$ and $1890\,\mathrm{S\,cm}^{-1}$ respectively, and a similar trend is observed in the doped powders (Figures 17 and 18), competitive with established TCOs.

Through hard X-ray photoelectron spectroscopy (HAXPES), we find further evidence to support this description of the defect chemistry of $ZnSb_2O_6$. At high photon energies (approaching 6 keV), we can exploit the greater photoionisation cross-section of Sb 5s states, which we know make up the conduction band minimum, allowing us to observe any filled conduction band states. Figure 7 shows
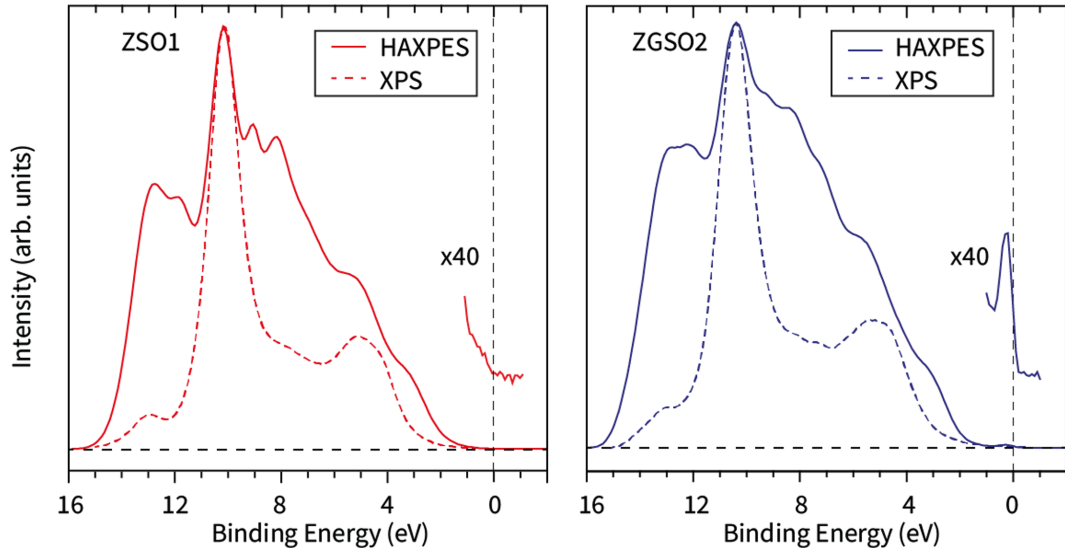
Figure 7: Valence band spectra of undoped (left, red) and Ga-doped (right, blue) $ZnSb_2O_6$ taken at a photon energy of 5.92 keV. Also overlaid is the soft X-ray spectrum of the same sample, at a photon energy of 1.48 keV. Inset shows a zoomed in view of the Fermi level, set to 0 eV.

the valence band spectra for undoped (left, red) and Ga-doped (blue, right) $ZnSb_2O_6$ aligned to the Fermi level of Au foil, with a zoom on the Fermi level shown in the inset for each spectrum. For the undoped system, there is no emission at 0 eV binding energy – i.e. there are no filled states. Upon Ga-doping, there is strong emission at 0 eV binding energy with a typical Fermi-Dirac-like distribution, indicating that the conduction band is populated with electrons, and the crystal displays degenerate conductivity.

2.4   Charge transport properties

Charge transport properties are important metrics in assessing the performance of prospective TCOs. Specifically, it is desirable for a TCO to possess high electron mobility in order to maximise conductivity. Figure 8a shows the experimental electron mobility of undoped and Ga-doped $ZnSb_2O_6$ single crystals over the temperature range 200 K to 350 K, where we observed an impressive room temperature mobility of $48.8\,cm^2\,V^{-1}\,s^{-1}$ at the maximum doping level ($2.4 \times 10^{20}\,cm^{-3}$), resulting in a conductivity of $1890\,S\,cm^{-1}$ (Figure 8c). Our THz domain spectroscopy (TDS) results on powder samples of Ga-doped $ZnSb_2O_6$ also demonstrate metallic-like conductivity in samples of up to 8% nominal Ga doping (Figures 17 and 18 in the SI). This is on par with many state of the art transparent conductors. Electron mobilities of $40\,cm^2\,V^{-1}\,s^{-1}$ to $60\,cm^2\,V^{-1}\,s^{-1}$ and conductivity on the order of $1 \times 10^4\,S\,cm^{-1}$ are common in thin films of ITO, FTO and AZO.[5,2,7]

To further understand the origin of the high mobility in $ZnSb_2O_6$, we performed charge transport calculations using the AMSET package.[36] This allowed us to calculate the limits to intrinsic mobility from various scattering mechanisms including polar optical phonons (POP), acoustic deformation potentials (ADP), and ionised impurities (IMP). We found that at low carrier concentrations, corresponding to the nominally undoped sample, polar optical phonon scattering dominates, while at higher concentrations the limiting scattering mechanism switches to ionised impurity scattering. This is demonstrated in Figure 8b, where the mobility of the undoped sample displays the strong temperature dependence typically associated with a system dominated by POP scattering, while at high carrier concentrations the mobility becomes largely temperature independent, indicative of IMP based scattering. In Figure 9, we explicitly plot the scattering rates at room temperature at both low and high carrier concentrations, clearly demonstrating this switch in the mobility limiting scattering mechanism.

There are some discrepancies between the experimental observations and simulations. First, our calculations predict that the nominally undoped material should exhibit a very high electron mobility

of around $70\,\mathrm{cm^2\,V^{-1}\,s^{-1}}$ at room temperature, and display a strong temperature dependence. However, our undoped sample shows the lowest mobility and only a weak temperature dependence. The trend of mobility with increased carrier concentration is in fact unclear across the whole batch of samples. Possible causes of these discrepancies include non-uniform distribution of the dopant during the CVT (chemical vapour transport) growth process, which would make extracting dopant concentration dependent charge transport properties less reliable; other unintentional impurities in the samples, increasing scattering rates; directional-dependence effects during measurement of the single crystals – the mobility of $ZnSb_2O_6$ has reasonable anisotropy, as shown in Figure 15. While alternative single crystal growth methods or the deposition of epitaxial thin films could provide further insight, the qualitative agreement between theory and experiment in this study demonstrates the feasibility and realisation of Ga-doped $ZnSb_2O_6$ as a transparent conducting oxide.
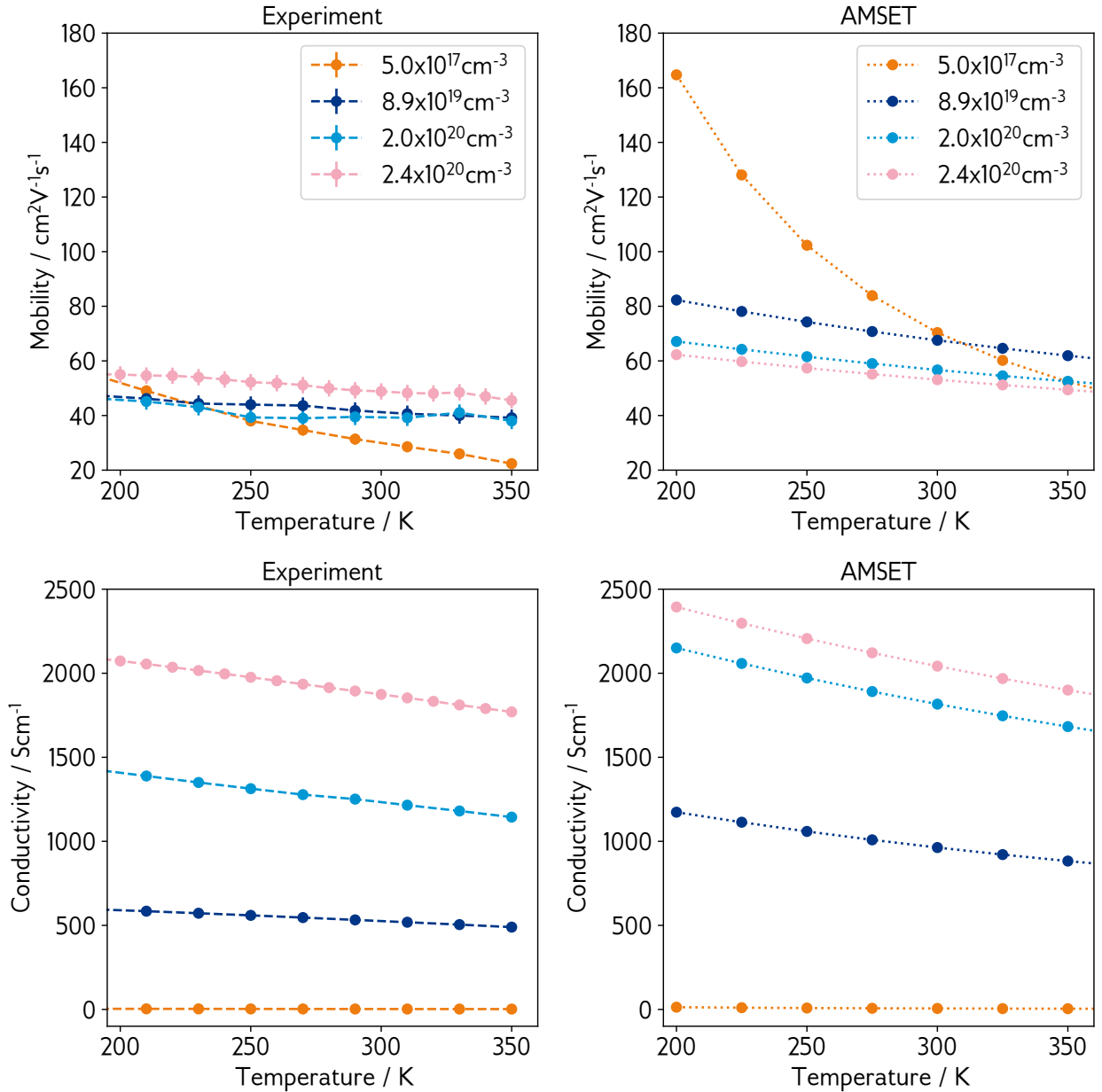

Figure 8: (a) Experimental and (b) simulated mobility and (c) experimental and (d) simulated conductivity of undoped and Ga-doped $ZnSb_2O_6$ in the temperature range $200\,\mathrm{K}$ to $350\,\mathrm{K}$. Measurements performed on single crystals.
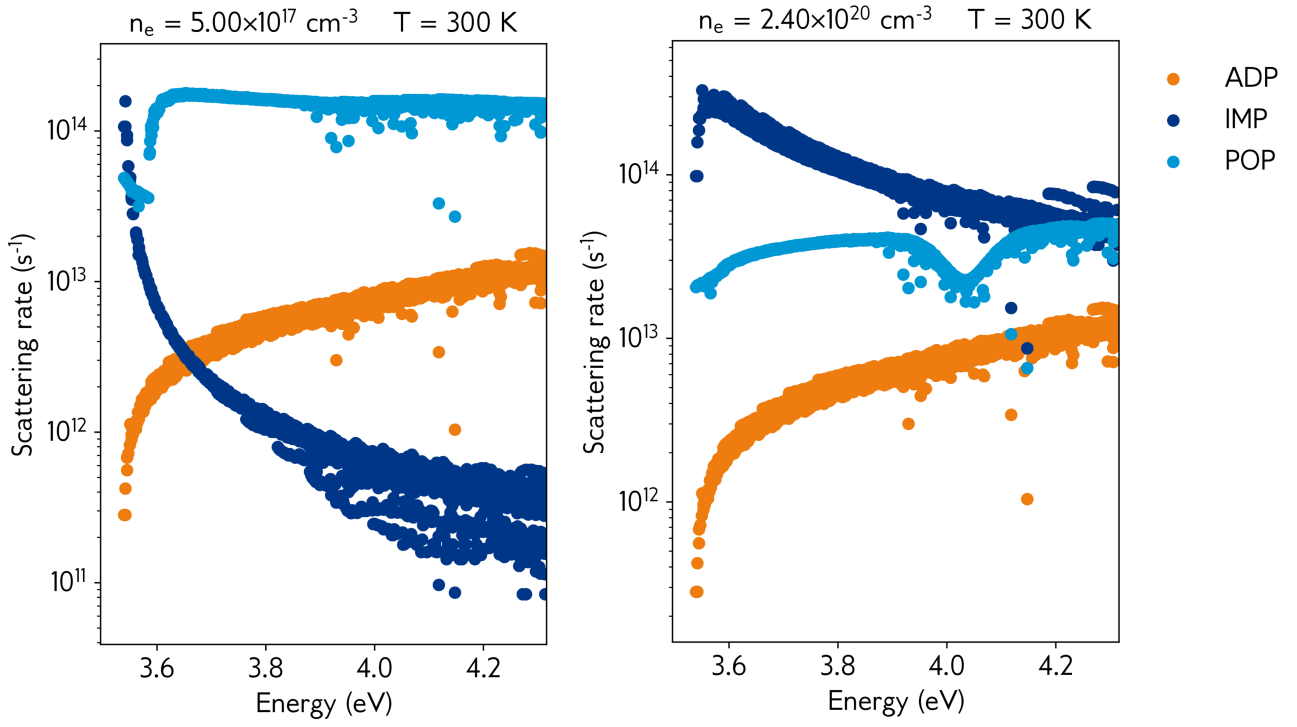
Figure 9: Room temperature simulated scattering rates at (a) $5.0 \times 10^{17}\,\mathrm{cm^{-3}}$ and (b) $2.4 \times 10^{20}\,\mathrm{cm^{-3}}$ charge carrier concentrations. ADP is acoustic deformation potential scattering, IMP is ionised impurity scattering, and POP is polar optical phonon scattering. Moving from low to high carrier concentrations causes a switch in dominant scattering from POP to IMP.
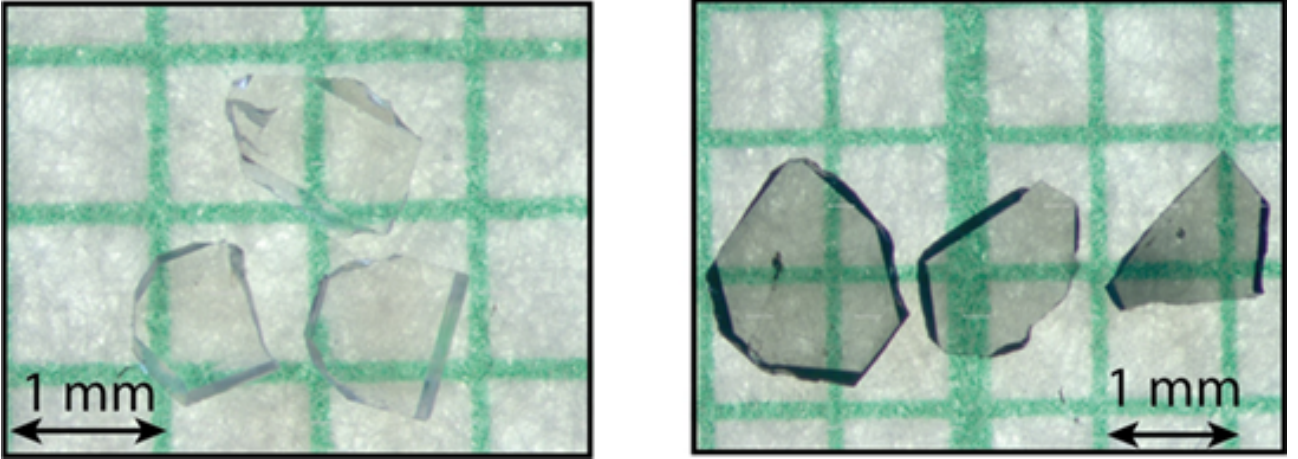
Figure 10: Optical image of CVT grown single crystals of undoped (left) and Ga-doped (right) $ZnSb_2O_6$. Each crystal has been polished to $150\,\mu m$ thickness.

2.5 Optical Properties

Images of undoped and Ga-doped $ZnSb_2O_6$ crystals are displayed in Figure 10, which have been polished to approximately $150\,\mu m$ thicknesses to aid visual comparison. The undoped samples are colourless and transparent, while the Ga-doped crystals display a blue tint. The transmission intensity $T(\%)$ of light through a material is given by the Beer-Lambert law $T(\lambda) = \exp(-\alpha_\lambda t)$, where α_λ is the absorption coefficient and t the sample thickness. For crystals polished down to a measurement-standard thickness of $150\,nm$, we report optical transmission greater than 99% for all samples, a significant improvement over the often reported $\sim 90\%$ transmission intensity for ITO thin films.[37] Table 2 summarises the optical data.

Table 2: Transmission data at $550\,nm$ with extracted absorption coefficient and calculated transmission at thickness $150\,nm$ and the extracted experimental band gaps in ZSO and ZSGO.

Sample	$T(550\,nm)$ $t\ 150\,\mu m$	$\alpha_\lambda\ cm^{-1}$ $\lambda\ 550\,nm$	$T(550\,nm)$ $t\ 150\,nm$	Direct-allowed band gap eV
Undoped	60.6%	13.1	99.98%	3.38 ± 0.02
1% doped	16.3%	108.1	99.83%	3.56 ± 0.02

The optical band gap of $ZnSb_2O_6$ rises from $3.38\,eV$, which is in excellent agreement with the direct gap value obtained from the hQSGW calculation, to $3.56\,eV$ upon nominal 1% Ga-doping in single crystals. This is indicative of the Moss-Burstein shift that is common among the degenerately doped TCOs. Figure 11 shows the experimentally derived band gaps from absorption measurements for both undoped and doped single crystals.

The experimental absorption coefficient is rather low, on the order of $300\,cm^{-1}$, compared to other TCOs. Investigation of the optical transition matrix from DFT calculations reveals that the VBM to CBM transition is forbidden, and the first strong onset is predicted to be from a band $0.72\,eV$ below the VBM (Figures 20 and 21 in the SI). Both experiment and theory point towards very low absorption in $ZnSb_2O_6$ below photon energies of $\sim 3.7\,eV$, possibly up to $4.25\,eV$. However, the thickness of the crystals causes the absorption coefficient to plateau above energies of $3.7\,eV$, preventing accurate measurement of the absorption coefficient above this energy and precluding observation of the predicted strong onset at around $4.25\,eV$, similar to the case in GeSe single crystals.[38] When polished down to thicknesses of $150\,nm$, our single crystals display transmission intensity greater than 99%, which supports the low absorption coefficient and symmetry forbidden nature of the direct gap, but a thin film deposition is required to probe this behaviour further.

Transmission data for the $150\,\mu m$ single crystal samples at a wavelength of $550\,nm$ can be found in Figure 19 of the SI, from which we derived the Haacke figure of merit, shown in Figure 12. This

indicates an extremely high figure of merit at micron thicknesses, and competitive values at thicknesses on the order of $\sim 100\,\text{nm}$.
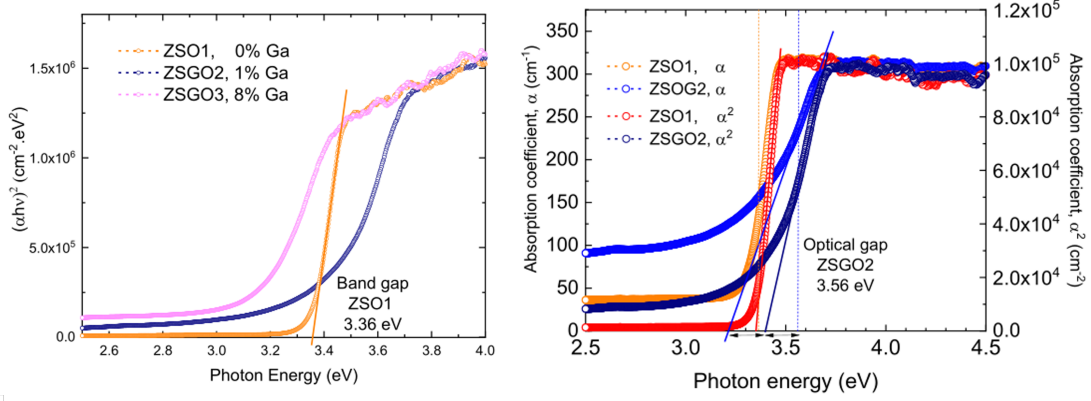

Figure 11: Absorption data and extracted band gaps for nominally undoped and 1% doped ZnSb_2O_6 single crystals, $t = 150\,\text{µm}$.
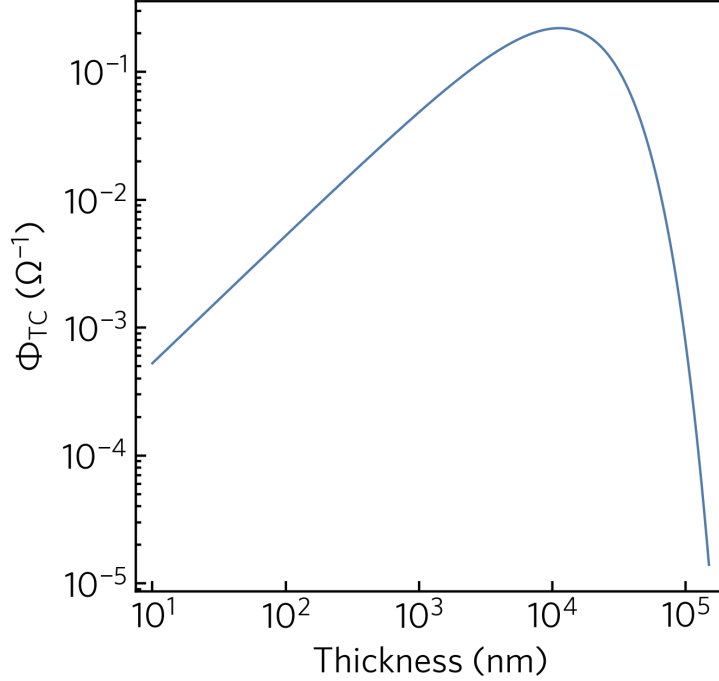

Figure 12: Haacke figure of merit data at transmittance wavelength of $550\,\text{nm}$.

2.6 Band alignment

In Figure 13, the calculated band alignment of ZnSb_2O_6 is shown, compared against commonly used TCOs. Our calculations reveal an ionisation potential (IP) and electron affinity (EA) of $9.6\,\text{eV}$ and $6.1\,\text{eV}$, respectively. Sb $5s$ states contribute strongly to the CBM, much like ns states in the other post-transition metal TCOs, but sit lower in energy due to the increased distance from the nucleus and improved shielding of effective charge by core electrons. Therefore, the EA of ZnSb_2O_6 is significantly greater than that of the industry leading TCOs. Upon Ga-doping, the Fermi level is predicted to sit above the conduction band minimum, which means a work function nearly $1\,\text{eV}$ larger than In_2O_3 could be achieved. This has tremendous implications in organic photovoltaics (OPVs) which rely entirely on the charge extraction capability of the positive and negative electrodes. Having a transparent
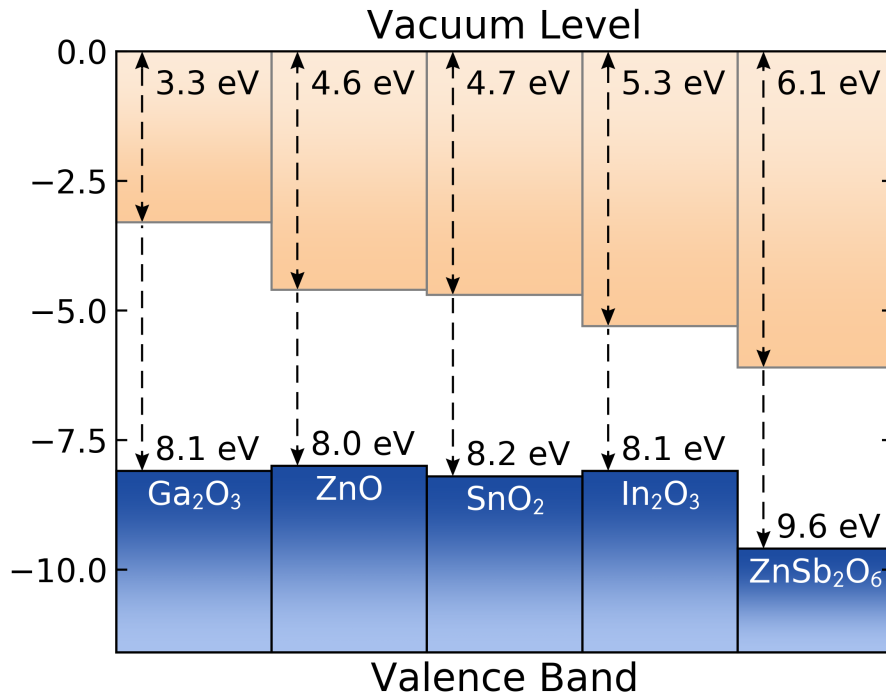
Figure 13: Band alignment of $ZnSb_2O_6$ compared against common TCOs. Ga_2O_3 from experiment,[39] ZnO, SnO_2 and In_2O_3 from theory.[34,40]

anode with a large electron affinity, and therefore work function, allows for closer band alignment to particularly low lying HOMOs (highest occupied molecular orbitals) in OPV devices, which can form stronger Ohmic contacts, increase the output voltage and drive up device efficiency.[41,42] Furthermore, replacing organic hole-extracting layers like PEDOT:PSS with a metal oxide like $ZnSb_2O_6$ could help to reduce the corrosion on the electrode.[43] To engineer large work functions in existing TCOs, modulation of the conduction band is required by alloying with heavy, and sometimes toxic, elements (for example $In_{2-x}Tl_xO_3$ and $Sn_{1-x}Pb_xO_2$)[34,44] – exploiting the native band alignment in $ZnSb_2O_6$ is a much cheaper, safer and easier way of incorporating a large work function material into devices.

3 Conclusion

We have used ab initio calculations to predict a new, earth abundant transparent conducting oxide $ZnSb_2O_6$, which we have successfully grown in single crystal form via chemical vapour transport. By studying the intrinsic and extrinsic defect chemistry, we were able to identify an effective doping strategy in order to realise degenerate conductivity through Ga-doping. We have used state-of-the-art packages to predict carrier concentrations and to calculate electron scattering rates, giving a more accurate prediction of charge transport properties that goes beyond the constant relaxation time approximation. Overall, we find good qualitative agreement between these predictions and our single crystals, with our best samples achieving carrier concentrations in excess of $2 \times 10^{20} \, \mathrm{cm^{-3}}$, electron mobility over $40 \, \mathrm{cm^2 \, V^{-1} \, s^{-1}}$ and conductivity of $1890 \, \mathrm{S \, cm^{-1}}$. The optical behaviour of Ga-doped $ZnSb_2O_6$ is also promising, with a direct band gap of around $3.4 \, \mathrm{eV}$ and optical transmittance greater than 99%. The next logical step is to develop a thin film deposition process for Ga-doped $ZnSb_2O_6$, in order to test its performance in typical device stacks and to better understand the relationship between charge carrier concentration, transport properties and optical band gap. Overall, this discovery is a significant milestone in the development of earth-abundant transparent conductors, offering a high-performance, low-cost alternative to industry standard materials, and opens the door to a whole family of Sb(V)-based transparent conducting oxides.

4 Methodology

4.1 Computational Methods

4.1.1 Geometry Optimisation and Electronic Structure

Density functional theory calculations were primarily performed within the plane-wave periodic code VASP,[45,46,47,48] which uses the projector augmented wave method to describe the interactions between valence and core states,[49,50] details of which can be found in Table 3. A plane-wave energy cut-off of $500\,\mathrm{eV}$ was used for all calculations, and a $7 \times 7 \times 4$ Γ-centred **k**-point mesh was employed. The PBE0[51,52] hybrid exchange correlation functional was used because it has been shown to accurately reproduce the band gap of rutile-structured SnO_2.[34,44,8] The static dielectric constant was calculated with density functional perturbation theory (DFPT) using the PBEsol functional.[53,54,55] Effective masses and band structures were calculated and plotted using the SUMO code.[56]

O	F	Al	Zn	Ga	Sb
$2s^2 2p^4$	$2s^2 2p^5$	$3s^2 3p^1$	$3d^{10} 4s^2$	$4s^2 4p^1$	$5s^2 5p^3$

Table 3: Explicitly treated valence electrons used in this work.

Additionally, a quasiparticle calculation was performed using the "hybrid quasiparticle self-consistent GW" (hQSGW) method as implemented in the QUESTAAL code using a linearised muffin-tin orbital (LMTO) basis set. In this hybrid approach a converged self-energy is obtained by the quasiparticle self-consistent GW (QSGW) approach, and an empirical 80% of the self-energy is combined with the LDA self-energy to obtain a prediction of the semiconductor bandgap.[57,58,59] This correction is routinely used to account for neglected interactions and improve the accuracy of bandgap estimations.[60,61] The lattice parameters and atomic positions were used from the results of the PBE0 geometry optimisation. The LMTO basis set was generated with the recommended parameters in QUESTAAL, using a $10\,\mathrm{Ry}^{1/2}$ cut-off for the interstitial mesh in the one-particle Hamiltonian steps, $2.7\,\mathrm{Ry}^{1/2}$ cut-off for the interstitial mesh of the two-particle objects and $3.3\,\mathrm{Ry}^{1/2}$ cut-off for the basis envelope functions in GW steps. The $7 \times 7 \times 4$ **k**-point grid used for the DFT calculations was reduced to $3 \times 3 \times 2$ for the GW steps. Effective masses were determined by quadratic fitting to band structure data, using tools in the QUESTAAL package.

4.1.2 Defect calculations

Stable competing phases with the Zn-Sb-O chemical potential space were relaxed using the PBE0 functional, a plane-wave energy cut-off of $500\,\mathrm{eV}$ and a converged **k**-point mesh until the forces were reduced to below $1 \times 10^{-2}\,\mathrm{eV\,\mathring{A}}^{-1}$. The ground state energies were used to identify the chemical potential limits that bound the thermodynamic stability of $ZnSb_2O_6$, using the program CPLAP.[32] The chemical potential of oxygen was set as the dependent variable in the CPLAP analysis, as this can be most readily changed in experiment through the use of partial pressures. The chemical potential limits from the thermodynamic stability calculations can be found in the SI.

A $2 \times 2 \times 1$ supercell (72 atoms) of the primitive cell was generated as an approximately cubic template for defect calculations ($9.35\,\mathring{A}$ by $9.35\,\mathring{A}$ by $9.26\,\mathring{A}$). There are two distinct cation sites in the $P4_2/mnm$ space group (Figure 1), one occupied by Zn (pale orange) and the other by Sb (dark orange) in $ZnSb_2O_6$, and two distinct anion sites (pale and dark blue), both occupied by O. Two interstitial candidate sites were identified: "i1" on the $8h$ Wyckoff site between two Zn and two Sb atoms, and "i2" on the $4c$ Wyckoff site between two Zn atoms. All supercells were optimised to reduce forces below $1 \times 10^{-2}\,\mathrm{eV\,\mathring{A}}^{-1}$, keeping the lattice vectors constant while allowing ionic coordinates to move. Supercell calculations were performed using a Γ-centred $2 \times 2 \times 2$ **k**-point mesh.

The Gibbs free energy of formation for each defect D with charge q in a given chemical environment μ and at a given Fermi energy E_F (relative to the VBM) is approximated as:[62]

$$\Delta G_f(D, q, \mu, E_F) = (E_{D,q} - E_{\text{host}}) + \sum_i n_i(E_i^{\text{ref}} + \mu_i) + q(E_F + \epsilon_{\text{VBM,host}}) + E_{\text{sc-corr}}(D, q). \quad (2)$$

To account for changes in composition n of each element i, the DFT total energy of a standard elemental reference E_i^{ref} is combined with a relative value of chemical potential μ_i. Post-processing supercell corrections are applied to counteract the effects of using a finite supercell, and consist of: potential alignment correction, to account for the shift in eigenvalues between a charged and non-charged supercell;[63] anisotropic image charge correction, developed by Murphy and Hine from the Makov-Payne method, a finite-size correction that removes the Coulombic repulsion between periodic images of defective supercells by treating the defect as a periodic point charge in a dielectric medium;[64,65] and a band filling correction, which counteracts the unrealistic filling of the conduction band (emptying of the valence band) in a finite-sized supercell.[63] At a given E_F, the lowest energy charge state dominates for that defect, and a "transition level" is the point at which two charge states are in thermodynamic equilibrium.

4.1.3 Charge Transport Calculations

Electronic transport properties were calculated using the AMSET package, which solves the linearised Boltzmann transport equation under the relaxation time approximation. Unlike the constant relaxation time approach, AMSET explicitly calculates band and **k**-dependent relaxation times using scattering matrix elements obtained from first principles inputs. Accordingly, AMSET can provide fundamental insights into the strength of scattering processes that limit charge transport, and has demonstrated excellent agreement with experimental measurements of mobility in a range of semiconductors.[36] In the present work, we have included scattering due to polar optical phonons (POP), acoustic deformation potentials (ADP), and ionised impurities (IMP). We have not included piezoelectric scattering as $ZnSb_2O_6$ is centrosymmetric ($4/mmm$ point group symmetry) and therefore does not display piezoelectricity. The primary input for AMSET was a hQSGW band structure calculation on a relatively dense $7 \times 7 \times 8$ **k**-point mesh. To calculate wave function overlaps, we used the wave function coefficients from a PBE0 calculation on the same k-point mesh, performed using VASP. The hQSGW and PBE0 computational methodologies were the same as described in the *"Geometry Optimisation and Electronic Structure"* section above. To obtain the transport properties and scattering rates, the electronic band structure and wave function coefficients were interpolated onto a dense $87 \times 87 \times 45$ k-point mesh. One benefit of AMSET compared to state-of-the-art approaches based on density functional perturbation theory combined with Wannier interpolation (DFPT+Wannier) is that scattering rates can be obtained from common materials parameters without requiring an expensive DFPT calculation.[66] The calculated materials parameters (dielectric constants, polar phonon frequency, and elastic constants) along with additional settings used by AMSET are provided in Section SX of the Supporting Information. The full AMSET methodology, including the scattering matrix elements and interpolation scheme is given in detail in Ref. 36.

4.1.4 Self Consistent Fermi Level Analysis

To calculate the SCFL of $ZnSb_2O_6$, a `python` based implementation of SC-FERMI was used (which can be found at `https://github.com/bjmorgan/py-sc-fermi`).[67] The required inputs are an electronic density of states of the defect-free system, a temperature, the total cell volume and number of electrons, and the thermodynamic transition levels for all defect species. The SCFL is calculated by recognising that the overall charge of a system must be equal to zero, which must be equal to the concentration of all of the charged defects plus any positive holes and negative electrons. We can construct simultaneous equations using the Fermi-Dirac distribution and the formation energy of a defect (Equation 2), and therefore find the Fermi level that gives overall charge neutrality. A rigorous description of this problem, and how it is implemented in the code, can be found in the original paper by John Buckeridge.[67]

In our analysis, we calculated the SCFL at the synthesis temperature of $ZnSb_2O_6$ and froze the defect concentrations at this temperature. We then recalculated the SCFL at room temperature,

allowing the concentration of the individual charge states of each defect to change, in order to predict the total electron concentration at the temperature at which our experiments were performed. A detailed `jupyter notebook` containing our calculation of the SCFL can be found in the online data repository.

4.1.5 Band alignment

The core level alignment method was used to calculate the ionisation potential and electron affinity of $ZnSb_2O_6$.[68] A slab-gap model was constructed using the PBE0 relaxed structure and a vacuum and slab thickness of $30\,\text{Å}$ using the SURFAXE code.[69] The (110) termination was selected, which has been demonstrated to be the lowest energy surface for rutile SnO_2.[70] The planar average of the electrostatic potential was converged and calculated within SURFAXE, and the plateau of this was taken to be the energy of the vacuum.

4.2 Experimental Methods

4.2.1 Solid State Synthesis

Powders of ZnO (Sigma-Aldrich, 4N), Sb_2O_3 (Sigma-Aldrich, 4N) and Ga_2O_3 (Sigma-Aldrich, 5N) were dried and ground together in near stoichiometric molar ratios. The powder was heated for 12 hours at $600\,°C$ in a $400\,\text{mbar}$ Ar atmosphere in a sealed quartz tube to pre-react to form the $ZnSb_2O_4$ phase. The 1-2-4 polycrystalline powder was then extracted, reground and heated in an air atmosphere at $800\,°C$ for a further 12 hours for oxidation into the $ZnSb_2O_6$ (1-2-6) phase. This two-step process was necessary to control antimony evaporation during baking,[14] and we typically observed less than 1% Sb loss during the synthesis which could be accurately accounted for by adding excess Sb_2O_3 in the starting materials.

Chemical vapour transport (CVT) was selected for the crystal growth method as it is appropriate for materials with high melting points and low vapour pressures such as ZnO[71] and Ga_2O_3.[72] Advantages include that high purity crystals can be obtained as, due to the closed nature of the growth system, minimal external impurities can be incorporated into the crystals. A sealed quartz ampule was employed using Cl_2 as a transport agent. The Cl_2 was added to the transport ampule via an evacuation rig similar to that described by Binnewies et al.[73] The tube was sealed at a length of $15\,\text{cm}$ and placed horizontally at the centre of a two-zone furnace set at $1100\,°C$ and $1000\,°C$. Since the reaction is endothermic the precursor was placed at the hot end of the ampule. After $200\,\text{hr}$, the powder was fully transported to the cold end in the form of single crystals adhered to the ampule walls. The ampule showed signs of attack during the growth reaction determined by XRD to be cristobalite (SiO_2), a feature not uncommon in CVT reactions using Cl_2 as a transport agent.[74] It is important to note EDS analysis shows no trace of silicon incorporated into the crystals. Gallium oxide also had a tendency to react with the ampule walls, and around 20% molar excess was added to the starting powders to compensate.

4.2.2 Characterisation

Samples were cut and polished into cuboid geometries with typical dimensions of $0.8\,\text{mm}$ by $0.6\,\text{mm}$ by $0.2\,\text{mm}$. The composition of the crystals was determined using an Oxford instruments energy-dispersive x-ray spectroscopy (EDS) system built into a JEOL JSM-6060OLV scanning electron microscope (SEM) operating at $20\,\text{keV}$, and the resultant data analysis using the Aztec software from Oxford Instruments. Electrical properties of the crystals were determined using a five-point Hall-bar geometry with Dupont silver-epoxy contacts annealed onto the bars allow Hall effect and resistivity measurements concurrently. Measurements were taken on a Quantum Design PPMS-9 using a $1\,\text{mA}$ excitation current in magnetic fields between $\pm\,1\,\text{T}$ at temperatures from $350\,\text{K}$ to $50\,\text{K}$. The Hall component of the transverse voltage V_{xy} was obtained by extracting the odd function dependence of the transverse resistance with an applied magnetic field. For optical measurements, a Shimadzu Solid UV-Vis-IR 3700 spectrophotometer was used to measure the transmittance of the crystals over the range of $250\,\text{nm}$ to $900\,\text{nm}$. Structural characterisation was made by x-ray diffraction measurements

on crushed crystals using a Rigaku SmartLab with a 9 kW rotating anode providing Cu Kα radiation. This arrangement employs a vertical goniometer and measured under a continuous scanning rate at 4 degrees per minute at 0.02° intervals of a 10° to 120° (2θ) range. X-ray photoemission spectroscopy (XPS) experiments were carried out using a Thermo K-alpha spectrometer utilising a 400 μm diameter Al Kα beam (1486.6 eV) equipped with a dual-beam Ar flood gun. The binding energies have been referenced to adventitious C 1s (284.8 eV). HAXPES measurements were carried out at the I09 beamline at Diamond Light Source Ltd, using a photon energy of 6 keV with a semi-grazing angle between the beam and sample of 11°. The binding energy scale and the experimental resolution of 250 meV were determined from Au foil in electrical contact with the sample.

Acknowledgements

Supplementary Information

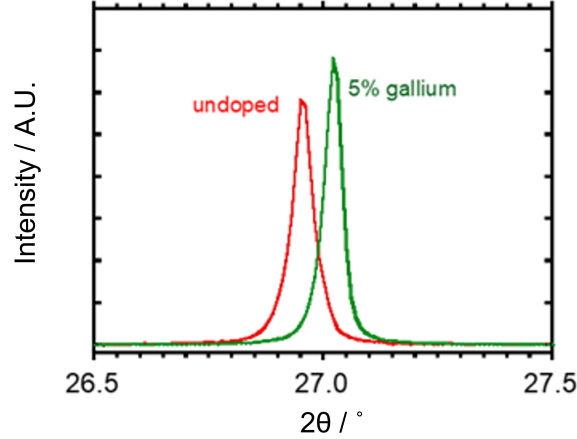Online repository of computational data can be found at DOI.

Figure 14: Systematic shift in Bragg peaks as a function of Ga-doping.

The chemical potential limits from the thermodynamic stability calculations can be found in Table 4 below.

	Sb	Zn	O	Al	Ga	F
A	-0.4661	-1.206	-1.9432	-5.1465	-2.2096	-3.1588
B*	-0.669	-1.6117	-1.808	-5.3493	-2.4124	-2.9559
C	-2.7628	-3.7055	-0.7611	-6.9196	-3.9828	-1.909
D	-4.6655	-4.4666	0	-8.0613	-5.1244	-1.5285
E	-5.3273	-3.143	0	-8.0613	-5.1244	-2.1903

Table 4: Chemical potential limits (in eV) of each element considered in this defect study. Asterisk denotes the limits used in the transition level diagrams in Figure 6.

All AMSET calculations were performed with the default settings, with the addition of free-carrier screening in the polar optical phonon matrix element (`free_carrier_screening: true`).

$$\text{High-frequency dielectric constant } (\epsilon_0) = \begin{bmatrix} 3.15 & 0 & 0 \\ 0 & 3.15 & 0 \\ 0 & 0 & 3.45 \end{bmatrix}$$

$$\text{Static dielectric constant } (\epsilon_0) = \begin{bmatrix} 12.16 & 0 & 0 \\ 0 & 12.16 & 0 \\ 0 & 0 & 8.86 \end{bmatrix}$$

$$\text{Elastic constant (GPa)} = \begin{bmatrix} 234 & 159 & 138 & 0 & 0 & 0 \\ 159 & 234 & 138 & 0 & 0 & 0 \\ 138 & 138 & 393 & 0 & 0 & 0 \\ 0 & 0 & 0 & 178 & 0 & 0 \\ 0 & 0 & 0 & 0 & 86 & 0 \\ 0 & 0 & 0 & 0 & 0 & 86 \end{bmatrix}$$

$$\text{Polar optical phonon frequency (THz)} = 10.767$$
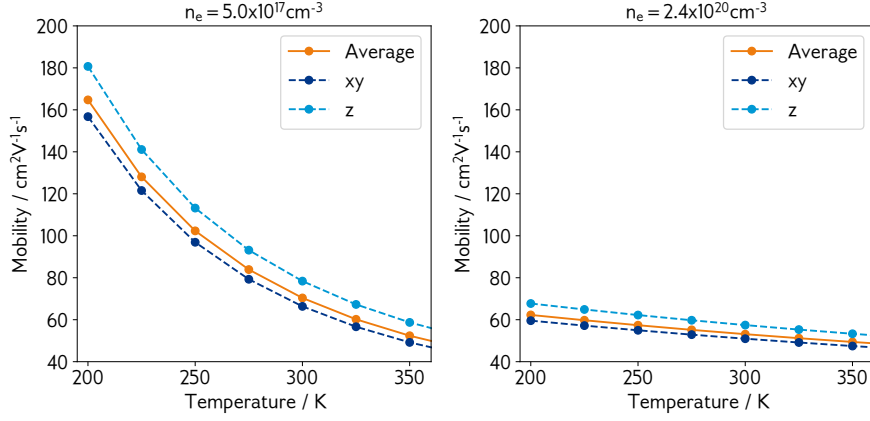
Directional mobilty plots from AMSET.

Figure 15: Directional mobility of $ZnSb_2O_6$ at room temperature at two different carrier concentrations.

4.2.3 Oxygen vacancies V_O

There are two distinct oxygen environments in $ZnSb_2O_6$, shown in Figure 16. In the first (light blue O atom), there are two equal Sb-O bonds of length $1.99\,\text{Å}$ and a single Zn-O bond of $2.07\,\text{Å}$. In the second, (dark blue O atom), the Sb-O bonds are of different lengths, $1.97\,\text{Å}$ for the Sb in the edge-sharing polyhedron and $1.98\,\text{Å}$ for the Sb in the corner-sharing polyhedron, while the Zn-O bond is longer at $2.09\,\text{Å}$. The formation energies of the neutral vacancy are $1.92\,\text{eV}$ and $1.98\,\text{eV}$, respectively, with both stabilising the +1 charge state for small Fermi level range ($0.03\,\text{eV}$ and $0.05\,\text{eV}$ respectively).
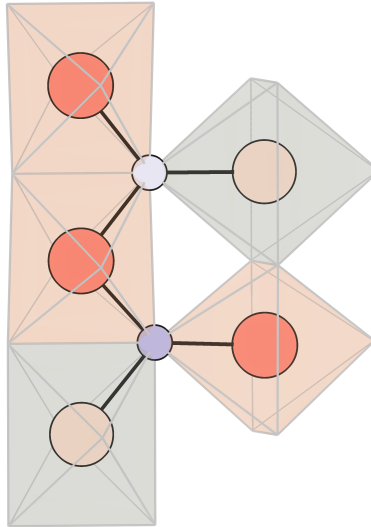

Figure 16: Local coordination environments of the two distinct oxygen atoms in $ZnSb_2O_6$. View is slightly offset from the a-axis.

In environment one, upon V_O generation, the two Sb atoms relax inwards by 2.6%, while the Zn relaxes outwards by 6.8%. Upon ionisation to V_O^+, the two Sb atoms relax outwards by 7.4% from their position in the neutral vacancy, and the Zn relaxes outwards by a further 0.7%. Ionising again to V_O^{++} causes a further 6.8% outwards relaxation of the Sb atoms and another 0.8% for the Zn atom.

In environment two, when the neutral vacancy forms, the Sb atom with the shorter bond length relaxes inwards by 10.9%, while the other Sb atom relaxes outwards by 3.7% and the Zn atom relaxes outwards by 8%. The Zn atom remains in approximately the same position regardless of charge state. Upon ionisation to V_O^+, the first Sb atom relaxes outwards again by 11.5%, surpassing its original position, while the other Sb atom relaxes outwards by a further 8.0%. Then after the second ionisation, the first Sb relaxes away by 13.5% and the second by a further 2.7%.

21

In both cases, Sb is preferentially attracted towards the neutral vacancy over Zn, presumably due to the higher charge on the cation and the smaller ionic radius. The relatively equally-sized steps in inward and outward relaxation as a function of charge state in both cases stabilises the narrow formation window of V_O^+ in $ZnSb_2O_6$, similar to what is observed in In_2O_3.[33] This is different to the negative-U behaviour observed in SnO_2 and ZnO,[34,35] which is driven by the much larger and non-stepwise change in bond lengths as a function of charge state.

4.2.4 THz spectroscopy

As synthesised Ga-doped $ZnSb_2O_6$ powder samples with nominal compositions of 2%, 8%, 10%, 15% and 20% Ga were measured using THz-domain spectroscopy (TDS) in order to obtain electrical conductivities. The spectrometer used a titanium sapphire laser as the source of ultrafast optical pulses (50 fs) with a wavelength of 800 nm. The generated pulses had a bandwidth of 0.3 THz to 3 THz, and the data was processed at 1 THz. Figures 17 and 18 show the electrical conductivity of these solid solutions at a range of temperatures, which are supporting of metallic-like conductivity upon Ga incorporation into the tri-rutile $ZnSb_2O_6$ structure.

Conductivity of the pure $ZnSb_2O_6$ sample is low at all temperatures, supportive of the defect chemistry that there are no shallow, intrinsic donors able to provide intrinsic, degenerate conductivity. As the nominal percentage of Ga increases, conductivity rises to a maximum around $1200\,\mathrm{S\,cm^{-1}}$, after which it begins to tail off. This is about 60% of the conductivity achieved in the most heavily doped single crystal. Considering the grain boundaries and extended defects present in powder samples, this is as expected.
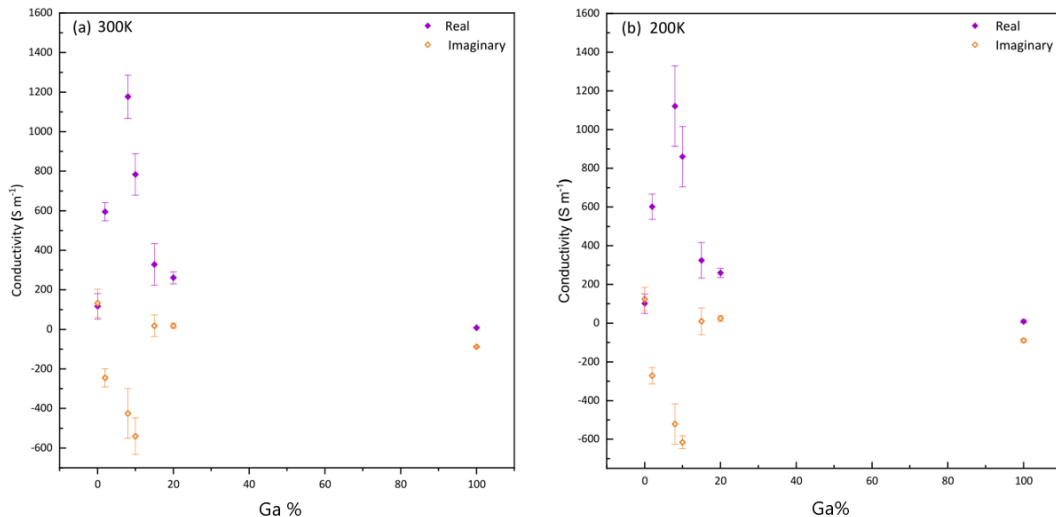

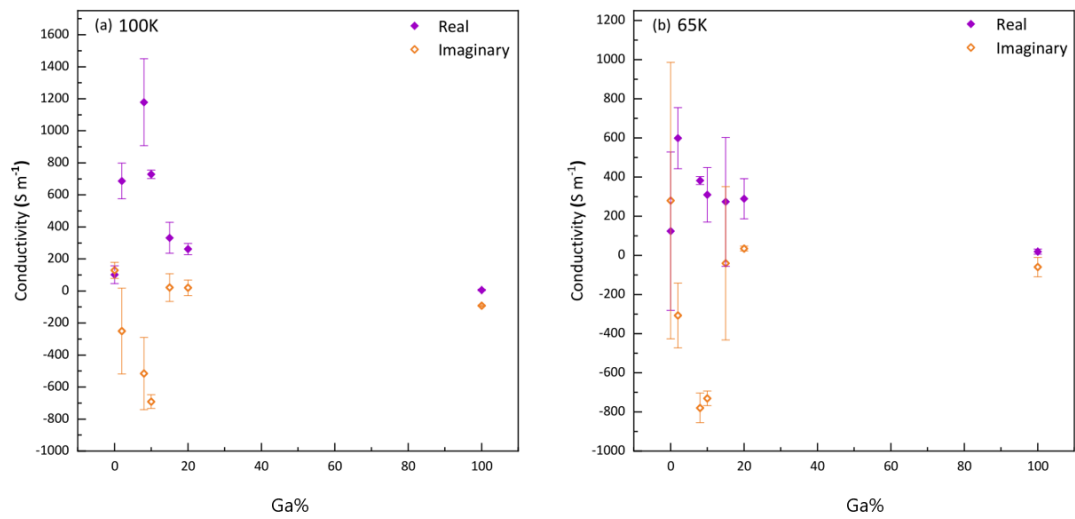Figure 17: TDS spectra of Ga-doped $ZnSb_2O_6$ powders at 300 K and 200 K.

22

Figure 18: TDS spectra of Ga-doped $ZnSb_2O_6$ powders at $100\,\text{K}$ and $65\,\text{K}$. Error bars become significantly larger at lower temperatures.
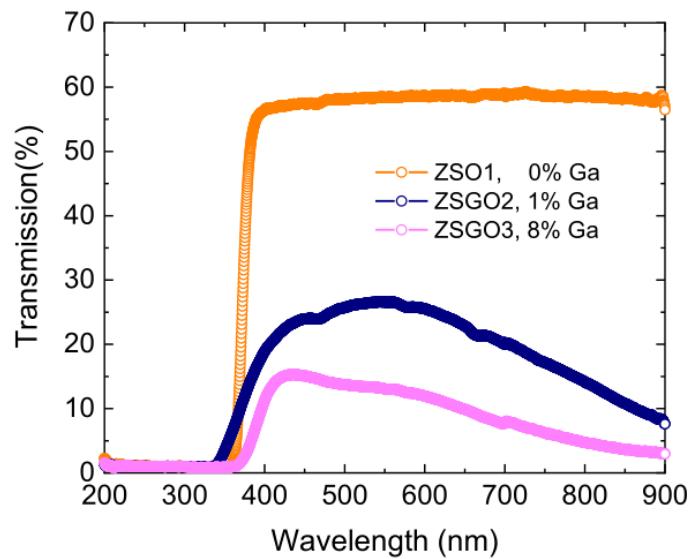

Figure 19: Transmittance data on single crystals polished to approximately $150\,\mu\text{m}$ thickness.
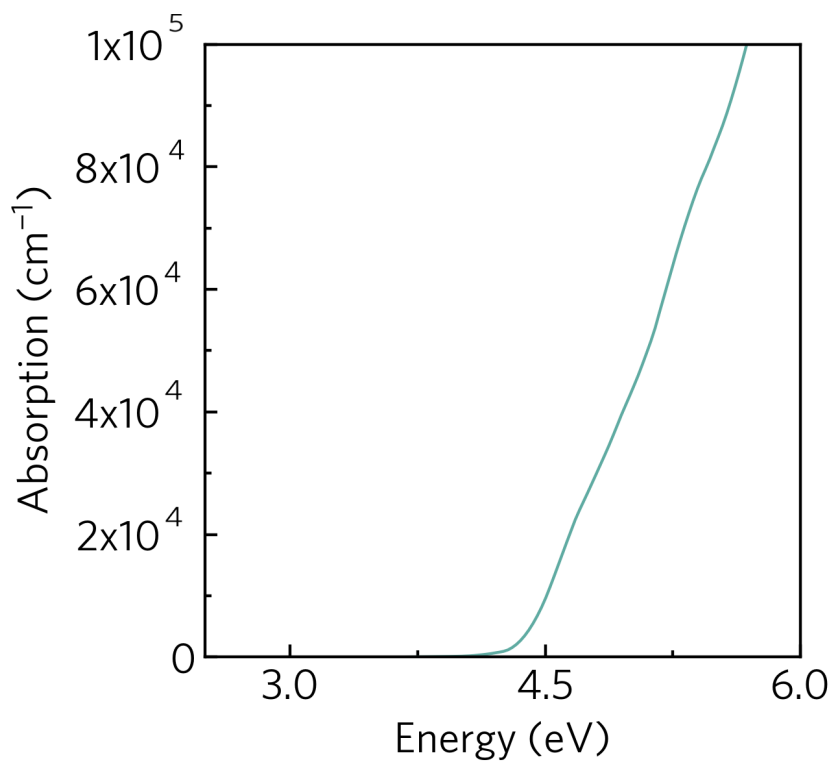
Figure 20: Calculated absorption spectrum of $ZnSb_2O_6$, showing a strong onset at around $4.2\,eV$, indicating that the fundamental direct transition from VBM to CBM ($3.53\,eV$) is in fact symmetry forbidden.
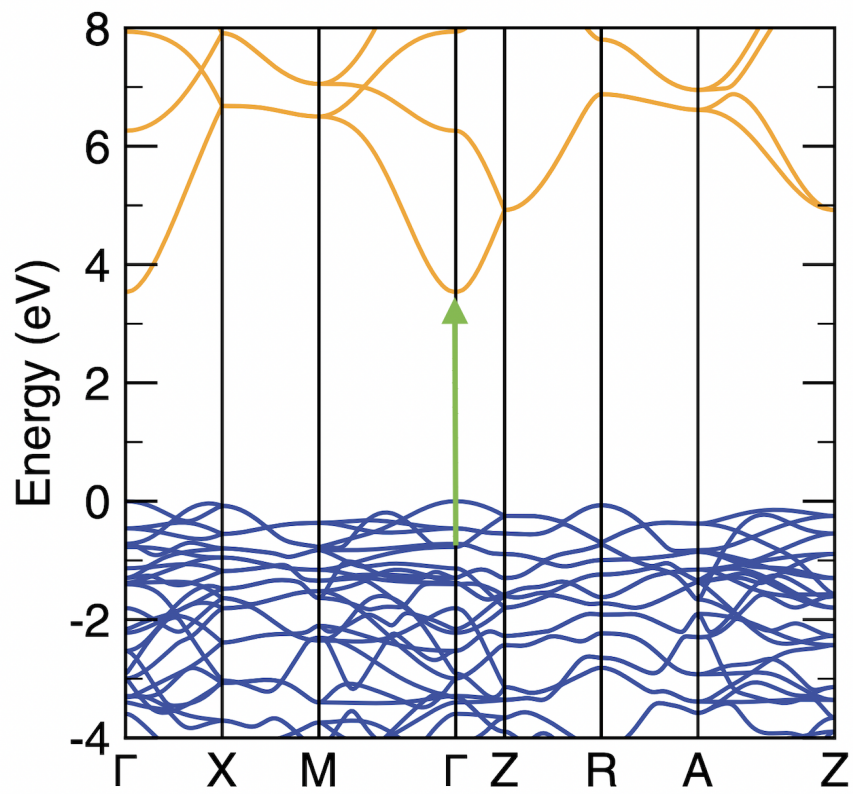
Figure 21: Optically allowed transition from $0.72\,\text{eV}$ belove the VBM to the CBM.

References

[1] C. Granqvist and A. Hultåker, *Thin Solid Films*, 2002, **411**, 1–5.

[2] J. E. N. Swallow, B. A. D. Williamson, T. J. Whittles, M. Birkett, T. J. Featherstone, N. Peng, A. Abbott, M. Farnworth, K. J. Cheetham, P. Warren, D. O. Scanlon, V. R. Dhanak and T. D. Veal, *Advanced Functional Materials*, 2017, **28**, 1701900.

[3] J. Li, S. Sathasivam, A. Taylor, C. J. Carmalt and I. P. Parkin, *RSC Advances*, 2018, **8**, 42300–42307.

[4] D. S. Bhachu, D. O. Scanlon, G. Sankar, T. D. Veal, R. G. Egdell, G. Cibin, A. J. Dent, C. E. Knapp, C. J. Carmalt and I. P. Parkin, *Chemistry of Materials*, 2015, **27**, 2788–2796.

[5] J. E. N. Swallow, B. A. D. Williamson, S. Sathasivam, M. Birkett, T. J. Featherstone, P. A. E. Murgatroyd, H. J. Edwards, Z. W. Lebens-Higgins, D. A. Duncan, M. Farnworth, P. Warren, N. Peng, T.-L. Lee, L. F. J. Piper, A. Regoutz, C. J. Carmalt, I. P. Parkin, V. R. Dhanak, D. O. Scanlon and T. D. Veal, *Materials Horizons*, 2020, **7**, 236–243.

[6] T. Koida, Y. Ueno and H. Shibata, *physica status solidi (a)*, 2018, **215**, 1700506.

[7] S. C. Dixon, S. Sathasivam, B. A. D. Williamson, D. O. Scanlon, C. J. Carmalt and I. P. Parkin, *Journal of Materials Chemistry C*, 2017, **5**, 7585–7597.

[8] B. A. D. Williamson, T. J. Featherstone, S. S. Sathasivam, J. E. N. Swallow, H. Shiel, L. A. H. Jones, M. J. Smiles, A. Regoutz, T.-L. Lee, X. Xia, C. Blackman, P. K. Thakur, C. J. Carmalt, I. P. Parkin, T. D. Veal and D. O. Scanlon, *Chemistry of Materials*, 2020, **32**, 1964–1973.

[9] H. J. Kim, U. Kim, H. M. Kim, T. H. Kim, H. S. Mun, B.-G. Jeon, K. T. Hong, W.-J. Lee, C. Ju, K. H. Kim and K. Char, 2012, **5**, 061102.

[10] L. Zhang, Y. Zhou, L. Guo, W. Zhao, A. Barnes, H.-T. Zhang, C. Eaton, Y. Zheng, M. Brahlek, H. F. Haneef, N. J. Podraza, M. H. W. Chan, V. Gopalan, K. M. Rabe and R. Engel-Herbert, *Nature Materials*, 2015, **15**, 204–210.

[11] C. Janowitz, V. Scherer, M. Mohamed, A. Krapf, H. Dwelk, R. Manzke, Z. Galazka, R. Uecker, K. Irmscher, R. Fornari, M. Michling, D. Schmeißer, J. R. Weber, J. B. Varley and C. G. V. de Walle, *New Journal of Physics*, 2011, **13**, 085014.

[12] R. Shannon, J. Gillson and R. Bouchard, *Journal of Physics and Chemistry of Solids*, 1977, **38**, 877–881.

[13] H. Mizoguchi and P. M. Woodward, *Chemistry of Materials*, 2004, **16**, 5233–5248.

[14] N. Kikuchi, H. Hosono, H. Kawazoe, O. Tanegashima, I. Ota and Y. Kimura, *Journal of the American Ceramic Society*, 2005, **88**, 2793–2797.

[15] J. Li, K. Du, Y. Lai, Y. Chen and Z. Zhang, *Journal of Materials Chemistry A*, 2017, **5**, 10843–10848.

[16] G.-X. Zhang, A. M. Reilly, A. Tkatchenko and M. Scheffler, *New Journal of Physics*, 2018, **20**, 063020.

[17] K. Momma and F. Izumi, *Journal of Applied Crystallography*, 2008, **41**, 653–658.

[18] A. Byström, B. Hök and B. Mason, *The crystal structure of zinc metantimonate and similar compounds*, Almqvist & Wiksell, 1941.

[19] S. Nishiyama and T. Hattori, *Journal of the Ceramic Society of Japan*, 2000, **108**, 435–438.

[20] R. D. Shannon, *Acta Crystallographica Section A*, 1976, **32**, 751–767.

[21] B. H. Toby and R. B. V. Dreele, *Journal of Applied Crystallography*, 2013, **46**, 544–549.

[22] G. Hautier, A. Miglio, D. Waroquiers, G.-M. Rignanese and X. Gonze, *Chemistry of Materials*, 2014, **26**, 5447–5458.

[23] Z. Lebens-Higgins, D. Scanlon, H. Paik, S. Sallis, Y. Nie, M. Uchida, N. Quackenbush, M. Wahila, G. Sterbinsky, D. A. Arena, J. Woicik, D. Schlom and L. Piper, *Physical Review Letters*, 2016, **116**, 027602.

[24] A. J. Jackson, A. M. Ganose, A. Regoutz, R. G. Egdell and D. O. Scanlon, *Journal of Open Source Software*, 2018, **3**, 773.

[25] J. Yeh and I. Lindau, *Atomic Data and Nuclear Data Tables*, 1985, **32**, 1–155.

[26] F. Oba, A. Togo, I. Tanaka, J. Paier and G. Kresse, *Phys. Rev. B*, 2008, **77**, 245202.

[27] S. K. Vasheghani Farahani, T. D. Veal, J. J. Mudd, D. O. Scanlon, G. W. Watson, O. Bierwagen, M. E. White, J. S. Speck and C. F. McConville, *Phys. Rev. B*, 2014, **90**, 1–9.

[28] N. F. Mott, *Reviews of Modern Physics*, 1968, **40**, 677–683.

[29] P. P. Edwards and M. J. Sienko, *Physical Review B*, 1978, **17**, 2575–2581.

[30] D. O. Scanlon, A. B. Kehoe, G. W. Watson, M. O. Jones, W. I. F. David, D. J. Payne, R. G. Egdell, P. P. Edwards and A. Walsh, *Physical Review Letters*, 2011, **107**, 246402.

[31] K. B. Spooner, A. M. Ganose and D. O. Scanlon, *Journal of Materials Chemistry A*, 2020, **8**, 11948–11957.

[32] J. Buckeridge, D. Scanlon, A. Walsh and C. Catlow, *Computer Physics Communications*, 2014, **185**, 330 – 338.

[33] I. Chatratin, F. P. Sabino, P. Reunchan, S. Limpijumnong, J. B. Varley, C. G. V. de Walle and A. Janotti, *Physical Review Materials*, 2019, **3**, 074604.

[34] D. O. Scanlon and G. W. Watson, *Journal of Materials Chemistry*, 2012, **22**, 25236.

[35] A. Janotti and C. G. V. de Walle, *Physical Review B*, 2007, **76**, 165202.

[36] A. M. Ganose, J. Park, A. Faghaninia, R. Woods-Robinson, K. A. Persson and A. Jain, *Nature Communications*, 2021, **12**, 2222.

[37] H. Kim, C. M. Gilmore, A. Piqué, J. S. Horwitz, H. Mattoussi, H. Murata, Z. H. Kafafi and D. B. Chrisey, *Journal of Applied Physics*, 1999, **86**, 6451–6461.

[38] P. A. E. Murgatroyd, M. J. Smiles, C. N. Savory, T. P. Shalvey, J. E. N. Swallow, N. Fleck, C. M. Robertson, F. Jäckel, J. Alaria, J. D. Major, D. O. Scanlon and T. D. Veal, *Chemistry of Materials*, 2020, **32**, 3245–3253.

[39] J. Zhang, J. Willis, Z. Yang, X. Lian, W. Chen, L.-S. Wang, X. Xu, T.-L. Lee, L. Chen, D. O. Scanlon and K. H. Zhang, *Cell Reports Physical Science*, 2022, 100801.

[40] B. Höffling, A. Schleife, C. Rödl and F. Bechstedt, *Physical Review B*, 2012, **85**, year.

[41] M. T. Greiner and Z.-H. Lu, *NPG Asia Materials*, 2013, **5**, e55–e55.

[42] W. Cao and J. Xue, *Energy & Environmental Science*, 2014, **7**, 2123.

[43] S. Kim, M. A. Saeed, S. H. Kim and J. W. Shim, *Applied Surface Science*, 2020, **527**, 146840.

[44] A. M. Ganose and D. O. Scanlon, *Journal of Materials Chemistry C*, 2016, **4**, 1467–1475.

[45] G. Kresse and J. Hafner, *Physical Review B*, 1993, **47**, 558–561.

[46] G. Kresse and J. Hafner, *Physical Review B*, 1994, **49**, 14251–14269.

[47] G. Kresse and J. Furthmüller, *Computational Materials Science*, 1996, **6**, 15–50.

[48] G. Kresse and J. Furthmüller, *Physical Review B*, 1996, **54**, 11169–11186.

[49] P. E. Blöchl, *Physical Review B*, 1994, **50**, 17953–17979.

[50] G. Kresse and D. Joubert, *Physical Review B*, 1999, **59**, 1758–1775.

[51] C. Adamo and V. Barone, *The Journal of Chemical Physics*, 1999, **110**, 6158–6170.

[52] J. Paier, R. Hirschl, M. Marsman and G. Kresse, *The Journal of Chemical Physics*, 2005, **122**, 234102.

[53] S. Baroni and R. Resta, *Physical Review B*, 1986, **33**, 7017.

[54] M. Gajdoš, K. Hummer, G. Kresse, J. Furthmüller and F. Bechstedt, *Physical Review B*, 2006, **73**, 045112.

[55] J. P. Perdew, A. Ruzsinszky, G. I. Csonka, O. A. Vydrov, G. E. Scuseria, L. A. Constantin, X. Zhou and K. Burke, *Physical Review Letters*, 2008, **100**, 136406.

[56] A. M. Ganose, A. J. Jackson and D. O. Scanlon, *Journal of Open Source Software*, 2018, **3**, 717.

[57] M. van Schilfgaarde, T. Kotani and S. Faleev, *Physical Review Letters*, 2006, **96**, 226402.

[58] A. N. Chantis, M. van Schilfgaarde and T. Kotani, *Physical Review Letters*, 2006, **96**, 086405.

[59] T. Kotani, M. van Schilfgaarde and S. V. Faleev, *Physical Review B*, 2007, **76**, 165106.

[60] A. Svane, N. E. Christensen, I. Gorczyca, M. van Schilfgaarde, A. N. Chantis and T. Kotani, *Physical Review B*, 2010, **82**, 115102.

[61] A. Punya and W. R. L. Lambrecht, *Physical Review B*, 2013, **88**, 075302.

[62] S. Lany and A. Zunger, *Physical Review B*, 2008, **78**, 235104.

[63] S. Lany and A. Zunger, *Modelling and Simulation in Materials Science and Engineering*, 2009, **17**, 084002.

[64] G. Makov and M. C. Payne, *Physical Review B*, 1995, **51**, 4014–4022.

[65] S. T. Murphy and N. D. M. Hine, *Physical Review B*, 2013, **87**, 094111.

[66] S. Poncé, W. Li, S. Reichardt and F. Giustino, *Reports on Progress in Physics*, 2020, **83**, 036501.

[67] J. Buckeridge, *Computer Physics Communications*, 2019, **244**, 329–342.

[68] S.-H. Wei and A. Zunger, *Applied Physics Letters*, 1998, **72**, 2011–2013.

[69] K. Brlec, D. W. Davies and D. O. Scanlon, *Journal of Open Source Software*, 2021, **6**, 3171.

[70] M. Batzill, K. Katsiev, J. M. Burst, U. Diebold, A. M. Chaka and B. Delley, *Physical Review B*, 2005, **72**, year.

[71] A. Mycielski, L. Kowalczyk, A. Szadkowski, B. Chwalisz, A. Wysmołek, R. Stepniewski, J. Baranowski, M. Potemski, A. Witowski, R. Jakieła, A. Barcz, B. Witkowska, W. Kaliszek, A. Jedrzejczak, A. Suchocki, E. Łusakowska and E. Kamińska, *Journal of Alloys and Compounds*, 2004, **371**, 150–152.

[72] H. Juskowiak and A. Pajaczkowska, *Journal of Materials Science*, 1986, **21**, 3430–3434.

[73] P. Schmidt, M. Binnewies, R. Glaum and M. Schmidt, in *P. Schmidt, M. Binnewies, R. Glaum and M. Schmidt*, InTech, 2013.

[74] J. Legma, G. Vacquier and A. Casalot, *Journal of Crystal Growth*, 1993, **130**, 253–258.